Article:

Middleton, T.A., Walker, R.T., Rood, D.H. et al. (6 more authors) (2016) The tectonics of the western Ordos Plateau, Ningxia, China: Slip rates on the Luoshan and East Helanshan Faults. Tectonics, 35 (11). pp. 2754-2777. ISSN 0278-7407

https://doi.org/10.1002/2016TC004230

Supporting Information for "The tectonics of the western Ordos Plateau, Ningxia, China: slip rates on the Luoshan and East Helanshan Faults"

Timothy A. Middleton,[1] Richard T. Walker,[1] Dylan H. Rood,[2] Edward J. Rhodes,[3] Barry Parsons,[1] Qiyun Lei,[4] Yu Zhou,[1] John R. Elliott,[1] and Zhikun Ren[5]

Corresponding author: Timothy A. Middleton, COMET, Department of Earth Sciences, University of Oxford, South Parks Road, Oxford, OX1 3AN, UK. (tim.middleton@earth.ox.ac.uk)

[1]COMET, Department of Earth Sciences, University of Oxford, South Parks Road, Oxford, OX1 3AN, UK

[2]Department of Earth Science and Engineering, Imperial College London, South Kensington Campus, London SW7 2AZ, UK & AMS Laboratory, Scottish Universities Environmental Research Centre, East Kilbride G75 0QF, UK

[3]Department of Geography, University of Sheffield, Sheffield, S10 2TN, UK

Contents of this file

1. Text S1 to S4

2. Figures S1 to S2

Introduction

1. Text S1. Pleiades DEM construction and offset measurement

We constructed high-resolution DEMs of the central portion of the Luoshan Fault and the southern end of the East Helanshan Fault using stereo pairs of Pleiades images. The images were processed using the Leica Photogrammetry Suite (LPS) module of the ERDAS Imagine software [*Parsons et al.*, 2014; *Zhou et al.*, 2015; *Middleton et al.*, 2015]. Tie points were used to compensate for orientation errors in the rational polynomial function (RPF) sensor model that approximates the relationship between image and ground coordinate systems. Having refined the RPF model, a pixel-by-pixel matching procedure was implemented with a window size of 9×9 pixels and a correlation coefficient of 0.3 to 0.7. Other parameters were tried, but this combination was found to give a good balance between point density and topographic smoothing. The apparent offset of a given

[4]Ningxia Seismological Bureau, Yinchuan, China

[5]State Key Laboratory for Earthquake Dynamics, Institute of Geology, China Earthquake Administration, Beijing, China

point on the ground between the two images was then triangulated in order to determine the three-dimensional position of that point. The resulting point cloud from pairwise matching was filtered by averaging within a block of 1 m and then gridded with a pixel spacing of 1 m (using the WGS84 ellipsoid and the UTM 48 N coordinate system) using continuous curvature splines in tension and a tension factor of 0.75. The imagery was then ortho-rectified using the Pleiades DEM.

Vertical offset measurements were made from these DEMs following the method of *Middleton et al.* [2015]. Swath profiles 10 to 20 m wide and at least 100 m long were taken from the raw Pleiades point cloud, perpendicular to the local fault trace and all points within this swath were projected onto a straight line. Separate straight lines were then fitted to the heights above and below the scarp with a simple least squares regression. Using the optical imagery to help identify unmodified fan surfaces, the data to fit was selected by hand, being careful to avoid vegetation and eroded channels. If the slope of the two lines differed by 1° or more, the profile was discarded since it was deemed not possible to adequately match the upper and lower surfaces in such cases. For the remaining profiles, parallel straight lines were then fitted to the data above and below the scarp in order to measure the vertical offset. The root mean square (RMS) residual in fitting these lines was then taken as the error on the offset measurement. The reliability of this method was previously tested by comparing the results to theodolite profiles measured in the field and by varying the swath width [*Middleton et al.*, 2015].

Horizontal offset measurements were made on the original Pleiades imagery and then checked on the DEMs and roughness maps where necessary. At any one sample location, straight lines were fitted by eye to either a channel thalweg or to the top or bottom of a terrace riser on both sides of the fault. The chosen feature to fit depended on its state of preservation and its clarity in the imagery. Where possible, terrace risers were used instead of channel thalwegs for highly sinuous channels. Up-slope risers that are less prone to post-offset channel erosion were preferred where possible [*Cowgill*, 2007]. We also made use of our field observations to guide our line fitting. We then measured the horizontal distance between the two piercing points, where these lines intersected our mapped fault trace. However, the aleatoric uncertainty associated with the individual measurement is much smaller than the epistemic uncertainty associated with the geomorphological reconstruction [*Scharer et al.*, 2014; *Elliott et al.*, 2015]. In our case, the aleatoric uncertainty is typically 0.5 m, as constrained by the pixel sizes in the Pleiades images, whereas the epistemic uncertainty can be as much as tens of metres in some instances. Therefore, in order to estimate realistic errors on our offset measurements, we combine measurements from sets of geomorphological features that appear to have been displaced by the same amount. This is done on the basis of field observations and by cutting the imagery along the fault trace and restoring one side of it to look for sets of features that all record the same offset. We then find the mean and 1σ standard deviation for each suite of offset measurements.

2. Text S2. IRSL dating

2.1. Background to IRSL dating

The decay of radioisotopes, typically ^{40}K, ^{238}U, ^{235}U, and ^{232}Th, within a sedimentary deposit causes electrons in individual mineral grains to be promoted from the valence band to the conduction band. Some of these energised electrons are trapped metastably by crystal defects. A small amount of additional energy from heat (thermoluminescence, TL), visible light (optically stimulated luminescence, OSL) or infrared radiation (infrared stimulated luminescence, IRSL) pushes the electrons out of these traps and they drop back down to the valence band, emitting photons in the process [*Burbank and Anderson*, 2012]. These electron traps are reset, or bleached, by brief heating at around 200 to 400 °C or exposure to daylight. The burial age of a sediment can therefore be determined by measuring the luminescence signal of a quartz or feldspar grain. The age of the deposit is equal to the equivalent dose (D_e), or total past radiation exposure, divided by the irradiation rate.

The technique that is most often employed is quartz OSL, as originally suggested by *Huntley et al.* [1985], and the commonly used method is the single aliquot regenerative dose (SAR) protocol of *Murray and Wintle* [2000]. This technique measures the natural luminescence signal of a sample aliquot (typically a few hundred grains). The same aliquot is then bleached, exposed to a known amount of radiation, and re-measured for luminescence a number of times so as to construct a growth curve. This allows the natural luminescence signal to be converted into an estimate of D_e [*Burbank and Anderson*, 2012].

Quartz OSL has been used successfully in numerous locations. However, some samples, particularly those containing grains recently eroded from bedrock, show low sensitivities and ages can be hard to determine. In other words, the luminescence signal generated per unit of radiation exposure is very low. Potassium feldspars (K-feldspars), however, typically have much higher sensitivities than quartz [*Rhodes*, 2011] and can therefore be used in more challenging sedimentary contexts. The disadvantage of K-feldspars, though, is that they can exhibit anomalous fading due to quantum mechanical tunnelling resulting in age underestimations.

Feldspar IRSL signals were first proposed for dating by *Hütt et al.* [1988]. Since K-feldspars have such high sensitivities, single-grain measurements yield D_e estimates for as many as 70 percent of grains [*Rhodes*, 2015]. An additional adjustment to the technique was proposed by *Buylaert et al.* [2009], whereby an initial controlled exposure to light can reduce or remove signals from grains that are most susceptible to anomalous fading. This is called post-IR IRSL signal measurement.

2.2. Methodology for IRSL dating

Samples for feldspar IRSL dating were collected in steel tubes, hammered into clean sediment sections. The samples were then prepared and analysed in the Department of Geography at the University of Sheffield under low intensity LEDs.

The samples were treated with dilute HCl to remove carbonates and then dry-sieved to 180-212 μm. K-feldspars were extracted by floatation in a centrifuge using lithium metatungstate solution with a density of 2.58 g/cm^3. The grains were then rinsed thoroughly and etched in 10 percent HF to remove their outer surfaces. Single-grain post-IR IRSL signal measurements were then made on each sample and fading assessments were conducted on each grain following D_e determinations. See *Rhodes* [2015] for a detailed discussion of the methods.

3. Text S3. ^{10}Be dating

3.1. Background to ^{10}Be dating

Cosmic rays produce in situ cosmogenic radionuclides, such as ^{10}Be, when they interact with the Earth's surface. The concentration of ^{10}Be in an object can therefore be used to determine the length of time that an object has been at the surface [*Hetzel*, 2013; *Benedetti and van der Woerd*, 2014]. The production rate (P_0) of ^{10}Be decays exponentially with depth over an e-folding length of 50-70 cm, so only the top few centimetres can be used for dating [*Burbank and Anderson*, 2012]. Since ^{10}Be is also radioactive its concentration at any one time in a surface object is a balance between the rate of production, the rate of decay and the erosion rate; at secular equilibrium the rate of production is equal to the rate of decay and the concentration of ^{10}Be equilibrates to the erosion rate [*Gosse and Phillips*, 2001; *Granger and Schaller*, 2014]. For ^{10}Be in quartz, secular equilibrium is reached after around 4 Ma [*Burbank and Anderson*, 2012].

A number of other factors must also be accounted for when using ^{10}Be concentrations for age determination of exposed surface objects. The local production rate varies from mineral to mineral. Typically quartz is used for analysis, since ^{10}Be is produced from ^{18}O, and ^{18}O is abundant in quartz; the production rate is 4.6 atoms of ^{10}Be per gram of quartz per year of exposure (at sea level in mid- to high latitudes) [*Burbank and Anderson*, 2012]. Since cosmic rays are steered by the Earth's magnetic field and absorbed by the Earth's atmosphere, both latitude and altitude must also be taken into account. Furthermore, nearby topography can shield a sample from cosmic rays, so a shielding factor must be calculated and corrected for [*Balco et al.*, 2008; *Hetzel*, 2013].

When dating depositional surfaces the primary concern is inheritance [*Benedetti and van der Woerd*, 2014]. During exhumation, transport within a hillslope system, transport within a fluvial system, and final deposition a rock sample will have been exposed to cosmic rays and will start to accumulate ^{10}Be. This inherited component can be estimated by measuring the concentration of ^{10}Be in pebbles from modern river channels. However, this assumes that rates of erosion and sediment transport don't vary over time, for example over glacial-interglacial cycles [*Schmidt et al.*, 2011]. Finally, post-depositional erosion (or soil inflation) can cause a sample to appear younger (or older) than it actually is; assuming no erosion gives a minimum exposure age. By picking samples from boulders with a dark desert varnish the effects of erosion can be minimised [*Schmidt et al.*, 2011].

3.2. Methodology for ^{10}Be dating

The measured concentration of ^{10}Be in the sample is typically very small, so quartz grains must be separated from the sample rock and the sample analysed in an accelerator mass spectrometer (AMS) [*Burbank and Anderson*, 2012].

Initial sample preparation was carried out in the Department of Earth Sciences at the University of Oxford. Samples were broken into fist-sized chunks with a rock splitter and then crushed with a steel jaw crusher. For samples comprising an amalgamation of quartz pebbles the pebbles were sieved, and where necessary split into smaller pieces, so that only pebbles in the size range 8 to 16 mm were included. Further grinding was done in a TEMA swing mill with a tungsten carbide bowl. The crushate was then sieved to obtain the 250 to 500 μm fraction and passed through a Frantz magnetic separator to remove magnetic minerals.

Quartz purification and ^{10}Be extraction was then completed at the Scottish Universities Environmental Research Centre (SUERC) in East Kilbride, outside Glasgow. Boulder top samples that did not consist of pure quartz underwent froth flotation to remove unwanted feldspars and micas. Be carrier was added to each sample before being dissolved in HF. The solution was evaporated and re-dissolved in HCl a number of times to eliminate residual fluorides. Be was then separated using ion exchange chromatography. Fe species were removed by anion exchange in HCl and Ti species were removed by cation exchange with dilute H_2SO_4. Be was then precipitated as beryllium hydroxide and ignited to beryllium oxide, mixed with Nb powder, and pressed into copper cathodes.

^{10}Be/^{9}Be ratios were measured by AMS at SUERC [*Xu et al.*, 2010]. All measurements were normalised to the standard NIST_ 27900, with an assumed ^{10}Be/^{9}Be ratio of 2.79 x 10^{-11}. Final exposure ages were calculated with the CRONUS-Earth online calculator (version 2.2) [*Balco et al.*, 2008], using a Be half-life of 1.36 Ma [*Nishiizumi et al.*, 2007] and the constant production rate model of [*Lal*, 1991] and [*Stone*, 2000]. Topographic shielding values were also calculated using the CRONUS-Earth calculator based on azimuths and angular elevations to the horizon that were measured at sampling sites in the field [*Balco et al.*, 2008]. We also assume zero erosion.

4. Text S4. Kinematic model

Consider a set of equidimensional blocks with sides of length a.

If the rate of (left-lateral) shearing across the blocks is U, then the vorticity (W) is initially equal to $\frac{U}{a}$. In general, the rate of rotation of a pinned block depends on the current width of the zone (y), which varies during the rotation:

$$\frac{d\theta}{dt} = W = \frac{U}{y} \tag{1}$$

After a finite rotation of θ, y is given by:

$$y = a \sin\theta + a \cos\theta \tag{2}$$

Therefore:

$$\frac{dy}{d\theta} = a \cos\theta - a \sin\theta \tag{3}$$

And:

$$\frac{d\theta}{dt} = \frac{U}{a \sin\theta + a \cos\theta} \tag{4}$$

And so:

$$\frac{dy}{dt} = \frac{dy}{d\theta}\frac{d\theta}{dt} = (a\cos\theta - a\sin\theta)\left(\frac{U}{a\sin\theta + a\cos\theta}\right) = U\left(\frac{\cos\theta - \sin\theta}{\cos\theta + \sin\theta}\right) \tag{5}$$

For an equidimensional block, the rate of widening of the zone ($\frac{dy}{dt}$) is therefore independent of the starting dimension of the block (a). However, the rate of widening does depend on the total finite rotation so far (θ).

For the Ordos block, the rate of left lateral shearing across the block is $\approx$ 5 mm/a. In the Weihe Graben, the angle between the southern margin of the Ordos block and the

Qinlingshan is $\approx 25\,°$. Therefore, at the present day, we would expect the rate of widening of the zone ($\frac{dy}{dt}$) to be ≈ 1.8 mm/a.

We can also calculate the expected rate of strike-slip motion on the eastern and western boundaries of the block (v):

$$v = \omega r = \frac{d\theta}{dt} \times \frac{a}{2} \tag{6}$$

Therefore:

$$v = \frac{U}{a\sin\theta + a\cos\theta} \times \frac{a}{2} = \frac{U}{2\,(\sin\theta + \cos\theta)} \tag{7}$$

The velocity difference (v_{diff}) across the block in the east-west direction is:

$$v_{diff} = 2v = \frac{U}{\sin\theta + \cos\theta} \tag{8}$$

For $U = 5$ mm/a and $\theta = 25\,°$, $v_{diff} = 3.8$ mm/a.

Imagine a second, identical block adjacent to the first. The rate of strike-slip motion between the two blocks is the same as the velocity difference across one of the blocks in the east-west direction (v_{diff}).

References

References

Balco, G., J. O. Stone, N. a. Lifton, and T. J. Dunai (2008), A complete and easily accessible means of calculating surface exposure ages or erosion rates from 10Be and 26Al measurements, *Quaternary Geochronology*, *3*(3), 174–195, doi: 10.1016/j.quageo.2007.12.001.

Benedetti, L. C., and J. van der Woerd (2014), Cosmogenic Nuclide Dating of Earthquakes, Faults, and Toppled Blocks, *Elements*, *10*, 357–362, doi:10.2113/gselements.10.5.357.

Burbank, D. W., and R. S. Anderson (2012), *Tectonic Geomorphology*, 2nd ed., 472 pp., Wiley-Blackwell, Chichester.

Buylaert, J. P., A. Murray, K. J. Thomsen, and M. Jain (2009), Testing the potential of an elevated temperature IRSL signal from K-feldspar, *Radiation Measurements*, *44* (5-6), 560–565, doi:10.1016/j.radmeas.2009.02.007.

Cowgill, E. (2007), Impact of riser reconstructions on estimation of secular variation in rates of strike slip faulting: Revisiting the Cherchen River site along the Altyn Tagh Fault, NW China, *Earth and Planetary Science Letters*, *254*, 239–255, doi:10.1016/j.epsl.2006.09.015.

Elliott, A. J., M. E. Oskin, J. Liu, and Y. Shao (2015), Rupture termination at restraining bends: The last great earthquake on the Altyn Tagh fault, *Geophysical Research Letters*, pp. 1–7, doi:10.1002/2015GL063107.

Gosse, J. C., and F. M. Phillips (2001), Terrestrial in situ cosmogenic nuclides: theory and application, *Quaternary Science Reviews*, *20* (14), 1475–1560, doi:10.1016/S0277-3791(00)00171-2.

Granger, D. E., and M. Schaller (2014), Cosmogenic Nuclides and Erosion at the Watershed Scale, *Elements*, *10*, 369–374, doi:10.2113/gselements.10.5.369.

Hetzel, R. (2013), Active faulting, mountain growth, and erosion at the margins of the Tibetan Plateau constrained by in situ-produced cosmogenic nuclides, *Tectonophysics*, *582*, 1–24, doi:10.1016/j.tecto.2012.10.027.

Huntley, D. J., D. I. Godfrey-Smith, and M. L. W. Thewalt (1985), Optical dating of sediments, *Nature*, *313*, 105–107.

Hütt, G., I. Jaek, and J. Tchonka (1988), Optical dating: K-feldspars optical response stimulation spectra, *Quaternary Science Reviews*, *7*, 381–385, doi:10.1016/0277-3791(88)90033-9.

Lal, D. (1991), Cosmic ray labeling of erosion surfaces: in situ nuclide production rates and erosion models, *Earth and Planetary Science Letters*, *104*, 424–439.

Middleton, T. A., R. T. Walker, B. Parsons, Q. Lei, Y. Zhou, and Z. Ren (2015), A major, intraplate, normal-faulting earthquake: the 1739 Yinchuan event in northern China, *Journal of Geophysical Research (Solid Earth)*, *121* (1), 293–320, doi:10.1002/2015JB012355.Received.

Murray, A. S., and A. G. Wintle (2000), Luminescence dating of quartz using an improved single-aliquot regenerative-dose protocol, *Radiation Measurements*, *32*, 57–73.

Nishiizumi, K., M. Imamura, M. W. Caffee, J. R. Southon, R. C. Finkel, and J. McAninch (2007), Absolute calibration of 10Be AMS standards, *Nuclear Instruments and Methods in Physics Research, Section B: Beam Interactions with Materials and Atoms*, *258* (2), 403–413, doi:10.1016/j.nimb.2007.01.297.

Parsons, B., Y. Zhou, J. Elliott, I. Barisin, and R. Walker (2014), Assessing the Ability of Pleiades Stereo Imagery to Determine Height Changes in Earthquakes: A Case Study for the El Mayor-Cucapah Epicentral Area, *AGU Fall Meeting Abstracts*.

Rhodes, E. J. (2011), Optically Stimulated Luminescence Dating of Sediments over the Past 200,000 Years, *Annual Review of Earth and Planetary Sciences*, *39* (1), 461–488, doi:10.1146/annurev-earth-040610-133425.

Rhodes, E. J. (2015), Dating sediments using potassium feldspar single-grain IRSL: Initial methodological considerations, *Quaternary International*, *362*, 14–22, doi:10.1016/j.quaint.2014.12.012.

Scharer, K. M., J. B. Salisbury, J. R. Arrowsmith, and T. K. Rockwell (2014), Southern San Andreas Fault Evaluation Field Activity: Approaches to Measuring Small Geomorphic Offsets–Challenges and Recommendations for Active Fault Studies, *Seismological Research Letters*, *85* (1), 68–76, doi:10.1785/0220130108.

Schmidt, S., R. Hetzel, F. Mingorance, and V. a. Ramos (2011), Coseismic displacements and Holocene slip rates for two active thrust faults at the mountain front of the Andean Precordillera (33S), *Tectonics*, *30* (5), n/a–n/a, doi:10.1029/2011TC002932.

Stone, J. O. (2000), Air pressure and cosmogenic isotope production, *Journal of Geophysical Research*, *105* (B10), 23,753–23,759.

Xu, S., A. B. Dougans, S. P. Freeman, C. Schnabel, and K. M. Wilcken (2010), Improved 10Be and 26Al-AMS with a 5MV spectrometer, *Nuclear Instruments and Methods in Physics Research Section B: Beam Interactions with Materials and Atoms*, *268* (7-8), 736–738, doi:10.1016/j.nimb.2009.10.018.

Zhou, Y., B. Parsons, J. R. Elliott, I. Barisin, and R. T. Walker (2015), Assessing the ability of Pleiades stereo imagery to determine height changes in earthquakes: A case study for the El Mayor-Cucapah epicentral area, *Journal of Geophysical Research (Solid Earth)*, *120*, 8793–8808, doi:10.1002/2015JB012358.Received.

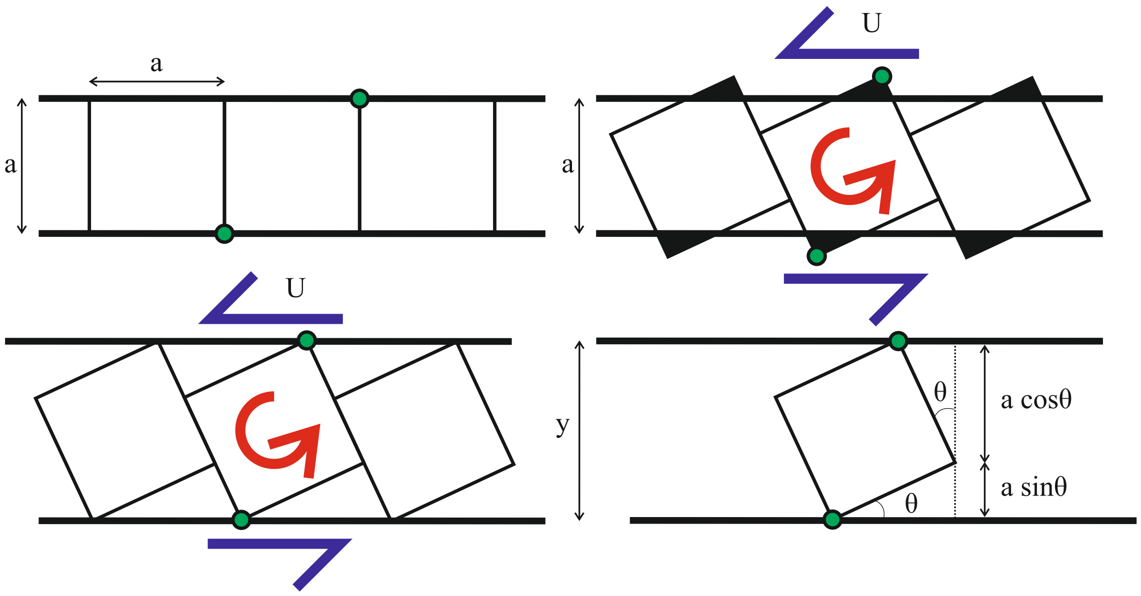

Figure 1. Block rotation cartoons, showing set-up of kinematic model described in Section S4. Cartoons show that for rotation to be accommodated, compression occurs at the corners of the blocks, or the overall zone has to widen.

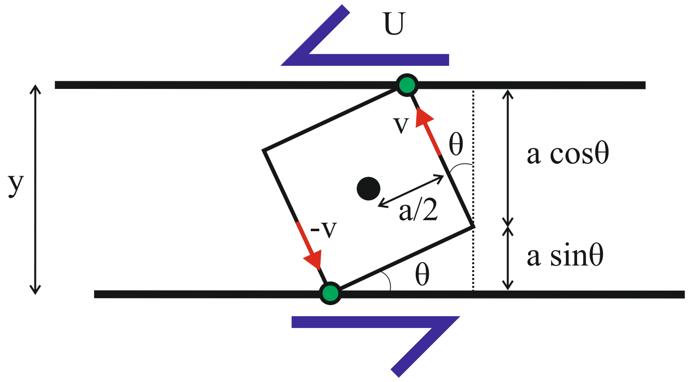

Figure 2. Second block rotation cartoon, showing parameters used to calculate v_{diff}, the east-west velocity difference across a block.